Towards completeness, a multiscale approach of confined particulate systems.

H.A. Meier[a], P. Steinmann[b] and E. Kuhl[c]

[a]Department of Mechanical Engineering,
University of Kaiserslautern, D-67653 Kaiserslautern, Germany.

[b]Department of Mechanical Engineering,
University of Erlangen-Nuremberg, D-91058 Erlangen, Germany.

[c]Department of Mechanical Engineering,
Stanford University, Stanford, CA 95305-4040, USA.

homei@rhrk.uni-kl.de, ps@rhrk.uni-kl.de, ekuhl@stanford.edu

Abstract: Numerical simulation and computational visualization of the failure characteristics of confined granular assemblies, e.g., sand, gravel or other types of loose aggregates, is the focal point of this publication. In general, standard continuum descriptions are exhausted if applied to loose granular materials, while discrete formulations fail to describe huge overall particulate structures. We propose a complete two scale homogenization procedure, including both a continuous and a discontinuous scale. Thus, we combine the capability of discrete methods to describe the behavior of the single grains and the possibility of a continuum approach to discretize the overall structure. Connections between the two scales are based on the concept of introducing a representative volume element on the discrete microscale. Driven by quantities from the macroscale, the representative volume element acts like a material law, returning the needed quantities to the continuous macro level. The particular challenge of this work lies in defining the connection between these two scales in terms of physical quantities and equations on the one hand and in terms of introducing appropriate visual tools which ultimately yield an improved understanding of these complex coupling mechanism on the other hand.

1 Introduction

Simulation of the distinguishing and complicated behavior of granular media calls for the mobilization of multiscale simulation techniques. While standard continuum methods strand by reproducing distinguishing behaviors, e.g., the breaking and forming of contacts between the grains, discrete methods are limited due to their computational costs. A multiscale combination of both methods leads to a powerful and efficient simulation tool. Thereby, a finite element method (fem) discretizes the overall structure on the ma-

croscale level. A discrete element method (dem) is used on the Gauss point level to simulate the behavior of the single grains. Connection between the two scales is based on the concept of introducing a representative volume element (rve) on the microscale level. This rve contains the discrete granular structure and acts as a material law for the macroscale level. The dem, introduced by [CS78, CS79], is suitable to capture the behavior of granular aggregates. In such a multiscale combination, the number of particles (nop) is limited inside the rve and the drawback of the dem disappears naturally. Studies pertaining the macroscopic stress and strain formulation are found in the publication of [KR96, KDHR00, DKHR01, EDM01, ERDD03].
This publication focuses on the introduction of a consistent tangent operator, allowing the use of an implicit solution scheme on the macroscale level. We restrict this contribution to the assumption of Taylor and Voigt, see [Voi89]. Thus, we do not consider any kind of micro fluctuations. All particles are mapped by the macroscopic deformation gradient tensor, leading to a homogeneous microscale deformation. The Piola stress as well as the consistent tangent operator are derived from the overall macroscopic energy, ab initio guaranteeing a major symmetry of the tangent operator.
The publication is segmented as follows: The calculation of the inter particle contact forces is presented in Section 2. Therefore, a force potential function is introduced which depends on the particle overlap. Section 3 concerns the homogenization process, based on the averaged macroscopic energy, resulting in the definition of the averaged macroscopic stress and tangent operator. To ensure the representativeness of the used volume element, a basic deformation rve study is outlined in Section 4. Uniformity of the initial contact network is compared by a contact normal density function and by characteristic error bar analyzes. A final example based on the well-known slope stability benchmark problem is illustrated in Section 5. Lastly, Section 6 closes with a final discussion.

2 Microscale - contact force

On the microscale level, the spatial position of each particle, $\boldsymbol{x}_i$ is described by a linear mapping of the initial particle position $\boldsymbol{X}_i$ by the macroscopic deformation gradient $\overline{\boldsymbol{F}}$.

$$\boldsymbol{x}_i = \overline{\boldsymbol{F}} \bullet \boldsymbol{X}_i \tag{1}$$

Individual particle fluctuations are ignored. This mapping, see (1), illustrates the assumption of Taylor and Voigt [Voi89], i.e., restricting the microscopic deformation to be homogeneous over the entire granular assembly. A comparable assumption was stated by Cauchy and Born in the context of continuum atomistics, see [Cau28a, Cau28b, Bor15]. The branch vector in the deformed configuration, $\boldsymbol{l}_{ij}$, connecting the center of particle i with the center of particle j, is received by subtracting the position vector of particle i from the position vector of particle j, see Fig. 1.

$$\boldsymbol{l}_{ij} = \boldsymbol{x}_j - \boldsymbol{x}_i = \overline{\boldsymbol{F}} \bullet \left[\boldsymbol{X}_j - \boldsymbol{X}_i\right] = \overline{\boldsymbol{F}} \bullet \boldsymbol{L}_{ij} \tag{2}$$

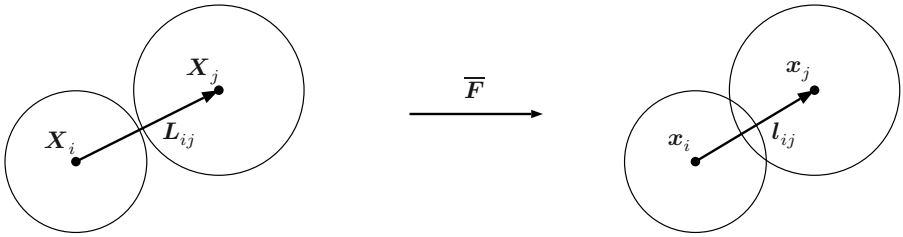

Figure 1: Initial and deformed configuration of the particles i and j. Left: Initial configuration with ε_{ij} less than zero. The branch vector $\boldsymbol{L}_{ij}$ connects the centers of the particles i and j. Right: Current configuration with an overlap ε_{ij} greater than zero. The particles i and j are in contact. The branch vector $\boldsymbol{l}_{ij}$ relates the two particle centers.

By subtracting the length of the branch vector $\left|\left|\boldsymbol{l}_{ij}\right|\right|$ from the sum of the particle radii, denoted by r_i and r_j, we obtain a description of the particle overlap.

$$\varepsilon_{ij} = r_i + r_j - \left|\left|\boldsymbol{l}_{ij}\right|\right| \tag{3}$$

Inspecting the definition of the particle overlap, we find ε_{ij} to have a positive or zero value in the case of contact. In this state, we allow the transfer of contact forces between the contacting grains. Accordingly, a negative value of ε_{ij} signals a gap of the size $|\varepsilon_{ij}|$. Clearly, (3) does not only represent the particle overlap, but also serves as an implicit contact check. Next, we introduce a force-potential function Φ_{ij} which depends on the overlap ε_{ij}, see, e.g., [MD04, Zoh05]. We require the force-potential function to be convex and its derivative monotonously increasing. Additionally, we demand its derivative to be zero for ε_{ij} being zero itself. Thus, we implicitly enforce the constraint $\varepsilon_{ij} < 0$.

$$\Phi_{ij} = \frac{E_{\mathsf{n}ij}}{2} \left[\mathscr{H}\left(\varepsilon_{ij}\right) \varepsilon_{ij}\right]^2 \tag{4}$$

The normal contact stiffness between the particles i and j is denoted by $E_{\mathsf{n}ij}$, whereas $\mathscr{H}$ expresses the Heaviside function. By letting the Heaviside function act on the particle overlap, the previous postulation and requirements are included in (4). Thus, our force-potential function describes a non-harmonic potential, solely delivering a value different from zero in the case of contact. Performing the derivative of (4) with respect to the position of particle i leads to the normal contact force $\boldsymbol{f}_{ij}$, acting on particle i.

$$\boldsymbol{f}_{ij} = -\frac{\mathrm{d}\Phi_{ij}}{\mathrm{d}\boldsymbol{x}_i} = -E_{\mathsf{n}ij}\mathscr{H}\left(\varepsilon_{ij}\right) \varepsilon_{ij} \boldsymbol{n}_{ij} \tag{5}$$

Therein, the magnitude of the contact force is given by $-E_{\mathsf{n}ij}\mathscr{H}\left(\varepsilon_{ij}\right) \varepsilon_{ij}$. The contact normal, pointing from the center of particle i to the center of particle j, is denoted by $\boldsymbol{n}_{ij} = \boldsymbol{l}_{ij} / \left|\left|\boldsymbol{l}_{ij}\right|\right|$. Using Newtons third law of reciprocal forces, the contact force acting on particle j equals $\boldsymbol{f}_{ji} = -\boldsymbol{f}_{ij}$. The complete particle assembly can be compared to

a network of linear springs, see [Hre41]. In contrast to the work of Hrennikoff, however, the contact network between the particles is developed and altered continuously during the simulation.

3 Macroscale - stress and tangent moduli

Our homogenization procedure is based on the well-known energy averaging theorem by Hill ([Hil72]), stating the equivalence between the volume average of the microscopic energy inside the rve and the macroscopic energy.

$$\overline{\Phi}\left(\overline{\boldsymbol{F}}\right) = \left\langle \Phi\left(\varepsilon_{ij}\left(\overline{\boldsymbol{F}}\right)\right)\right\rangle = \frac{1}{2\mathsf{V}_{\mathsf{rve}}} \sum_{i=1}^{\mathsf{nop}} \sum_{\substack{j=1 \\ j\neq i}}^{\mathsf{nop}} \Phi_{ij}\left(\varepsilon_{ij}\right), \tag{6}$$

where $\mathsf{V}_{\mathsf{rve}}$ denotes the volume of the rve in the undeformed reference configuration and

$$\begin{aligned} \left\langle \Phi\left(\overline{\boldsymbol{F}}\right)\right\rangle &= \frac{1}{4\mathsf{V}_{\mathsf{rve}}} \sum_{i=1}^{\mathsf{nop}} \sum_{\substack{j=1 \\ j\neq i}}^{\mathsf{nop}} E_{\mathsf{n}ij} \left[\mathscr{H}\left(\varepsilon_{ij}\right) \varepsilon_{ij}\right]^2 \\ &= \frac{1}{4\mathsf{V}_{\mathsf{rve}}} \sum_{i=1}^{\mathsf{nop}} \sum_{\substack{j=1 \\ j\neq i}}^{\mathsf{nop}} E_{\mathsf{n}ij} \mathscr{H}\left(\varepsilon_{ij}\right) \left[r_i + r_j - \left|\left|\overline{\boldsymbol{F}} \bullet \boldsymbol{L}_{ij}\right|\right|\right]^2. \end{aligned} \tag{7}$$

Based on the selected summation limits, each particle contact is considered twice. A multiplication by a factor of one half corrects the averaged energy output. At this point it is obvious that the volume averaged microscopic energy solely relies on the macroscopic deformation gradient. Insertion of (3) and (4) into (6) leads to the result presented in (7). The macroscopic Piola stress $\overline{\boldsymbol{P}}$ is obtained by taking the derivative of the averaged microscopic energy with respect to the macroscopic deformation gradient tensor.

$$\overline{\boldsymbol{P}}\left(\overline{\boldsymbol{F}}\right) = \frac{\mathrm{d}\left\langle \Phi\left(\overline{\boldsymbol{F}}\right)\right\rangle}{\mathrm{d}\overline{\boldsymbol{F}}} \tag{8}$$

with

$$\begin{aligned} \overline{\boldsymbol{P}}\left(\overline{\boldsymbol{F}}\right) &= \frac{1}{4\mathsf{V}_{\mathsf{rve}}} \sum_{i=1}^{\mathsf{nop}} \sum_{\substack{j=1 \\ j\neq i}}^{\mathsf{nop}} E_{\mathsf{n}ij} \frac{d\mathscr{H}\left(\varepsilon_{ij}\right) \left[r_i + r_j - \left|\left|\overline{\boldsymbol{F}} \bullet \boldsymbol{L}_{ij}\right|\right|\right]^2}{d\overline{\boldsymbol{F}}} \\ &= -\frac{1}{2\mathsf{V}_{\mathsf{rve}}} \sum_{i=1}^{\mathsf{nop}} \sum_{\substack{j=1 \\ j\neq i}}^{\mathsf{nop}} E_{\mathsf{n}ij} \mathscr{H}\left(\varepsilon_{ij}\right) \varepsilon_{ij} \boldsymbol{n}_{ij} \otimes \boldsymbol{L}_{ij}. \end{aligned} \tag{9}$$

In this, $\boldsymbol{n}_{ij} = \overline{\boldsymbol{F}} \bullet \boldsymbol{L}_{ij} / \left|\left| \overline{\boldsymbol{F}} \bullet \boldsymbol{L}_{ij} \right|\right|$ represents the unit contact normal vector in the current configuration. Using (5) we can rewrite (9) in a compact form,

$$\overline{\boldsymbol{P}}\left(\overline{\boldsymbol{F}}\right) = \frac{1}{2\mathsf{V}_{\mathsf{rve}}} \sum_{i=1}^{\mathsf{nop}} \sum_{\substack{j=1 \\ j \neq i}}^{\mathsf{nop}} \boldsymbol{f}_{ij} \otimes \boldsymbol{L}_{ij}, \tag{10}$$

solely consisting of the normal contact forces of the current configuration as well as the branch vector of the initial configuration. Taking the second derivative of the volume averaged microscopic energy with respect to the macroscopic deformation gradient, one obtains the fourth order algorithmic tangent operator $\overline{\mathbb{A}}$. As in classical structural mechanics, a split into a purely geometric and material part is possible. We can observe that non-linearity due to changes inside the contact network are directly reflected onto the material part of the tangent operator.

$$\overline{\mathbb{A}}\left(\overline{\boldsymbol{F}}\right) = \frac{\mathrm{d}^2 \left\langle \Phi\left(\overline{\boldsymbol{F}}\right)\right\rangle}{\mathrm{d}\overline{\boldsymbol{F}} \otimes \mathrm{d}\overline{\boldsymbol{F}}} = \frac{\mathrm{d}\overline{\boldsymbol{P}}\left(\overline{\boldsymbol{F}}\right)}{\mathrm{d}\overline{\boldsymbol{F}}} = \overline{\mathbb{A}}^{\mathsf{geo}}\left(\overline{\boldsymbol{F}}\right) + \overline{\mathbb{A}}^{\mathsf{mat}}\left(\overline{\boldsymbol{F}}\right) \tag{11}$$

with

$$\begin{aligned}
\overline{\mathbb{A}}^{\mathsf{geo}}\left(\overline{\boldsymbol{F}}\right) &= -\frac{1}{2\mathsf{V}_{\mathsf{rve}}} \sum_{i=1}^{\mathsf{nop}} \sum_{\substack{j=1 \\ j \neq i}}^{\mathsf{nop}} \frac{\mathscr{H}\left(\varepsilon_{ij}\right) E_{\mathsf{n}ij}}{\left|\left|\boldsymbol{l}_{ij}\right|\right|} \varepsilon_{ij} \mathbf{1} \overline{\otimes} \left[\boldsymbol{L}_{ij} \otimes \boldsymbol{L}_{ij}\right] \\
\overline{\mathbb{A}}^{\mathsf{mat}}\left(\overline{\boldsymbol{F}}\right) &= \frac{1}{2\mathsf{V}_{\mathsf{rve}}} \sum_{i=1}^{\mathsf{nop}} \sum_{\substack{j=1 \\ j \neq i}}^{\mathsf{nop}} \frac{\mathscr{H}\left(\varepsilon_{ij}\right) E_{\mathsf{n}ij}}{\left|\left|\boldsymbol{l}_{ij}\right|\right|} \left[r_i + r_j\right] \left[\boldsymbol{n}_{ij} \otimes \boldsymbol{n}_{ij}\right] \overline{\otimes} \left[\boldsymbol{L}_{ij} \otimes \boldsymbol{L}_{ij}\right]
\end{aligned} \tag{12}$$

Please note the special dyadic product, $\{\bullet \overline{\otimes} \circ\}_{abcd} = \{\bullet\}_{ac} \otimes \{\circ\}_{bd}$, enforcing the major symmetry of $\overline{\mathbb{A}}$. As with the macroscopic Piola stress, the algorithmic tangent operator solely depends on the macroscopic deformation gradient tensor.

4 Microscale - discrete element method

To select the appropriate rve, we call on a contact normal density function. This density function is used as a measure of uniformity and is outlined in [MSW$^+$07]. Yet, the contact density function promises a deeper insight with respect to the uniformity of the contact network. The rves, generated by the algorithm presented in [MKS07], are based on the grain size distribution shown in Fig. 2. Intrinsically, all generated rves include a geometric periodic boundary, a scaled grains size distribution and an unstructured particle network. We select a grain size distribution for quartz sand as shown in Fig. 2 and generate five rves for a number of 70, 350 and 700 primary particles, depicted in Fig. 3. Corresponding contact normal density functions are located beneath each rve, where we selected angles

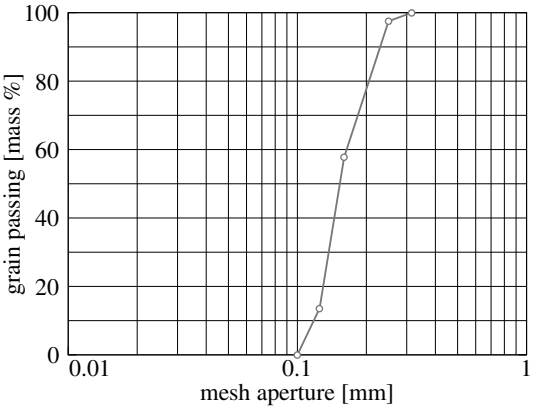

Figure 2: Typical grain size distribution for quartz sand used for rve generation. The grain passing in mass percent over mesh aperture is depicted. The abscissa shows the mesh aperture in [mm], whereas the ordinate reads the grain passing in volume percent.

of influence equal to 10°, 20° and 30°. One can observe that a wider angle of influence smooths the density function, while a smaller angle of influence results into a rather ruff output. Additionally, we find that a larger nop leads to a more uniform contact density function. The first two sets of rves, including each 70 and 350 primary particles, show a strong variation between the produced contact density functions. Instead, the rves including 700 primary particles show a good uniformity. A superior agreement of the contact density functions is found for the third rve of set three. Thus, this rve is considered to behave in an isotropic manner for small deformations. In contrast, the third rve of set one will show an anisotropic behavior. Next, our interest is focused on applying uniaxial compression as well as simple shear on each rve. The produced error bar plots, showing entries of the Cauchy stress versus the corresponding components of the deformation gradient, are depicted in Fig. 4 and 5. While the compression test shows a good overall agreement for all rves, the results of the simple shear test differ significantly. In case of the compression test, a linear stress behavior in the loading direction is observed, while in the orthogonal direction a nonlinear behavior is noticed. It is remarkable that for different nop the stress in the direction orthogonal to the direction of compression seems to converge towards a fixed value. Similar convergence is seen in the plot depicted in Fig. 5. In the case of the simple shear deformation a size reduction of the error bars, correlating to the increase of nop, is noticed. Thus, we can conclude that for an unlimited nop the error bars will tend towards a negligible value, e.g., an almost uniform behavior can be expected. Please note, the coarse scale smoothness of the depicted stress curves is strongly related to the Taylor assumption. Therefore, if fluctuations on the microscale are considered, a non-smooth coarse scale behavior of the stress is observed, see [MD04, Det06]. Nevertheless, fine scale non-smoothness is observed in both approaches. This observation is linked to minor changes inside the contact network.

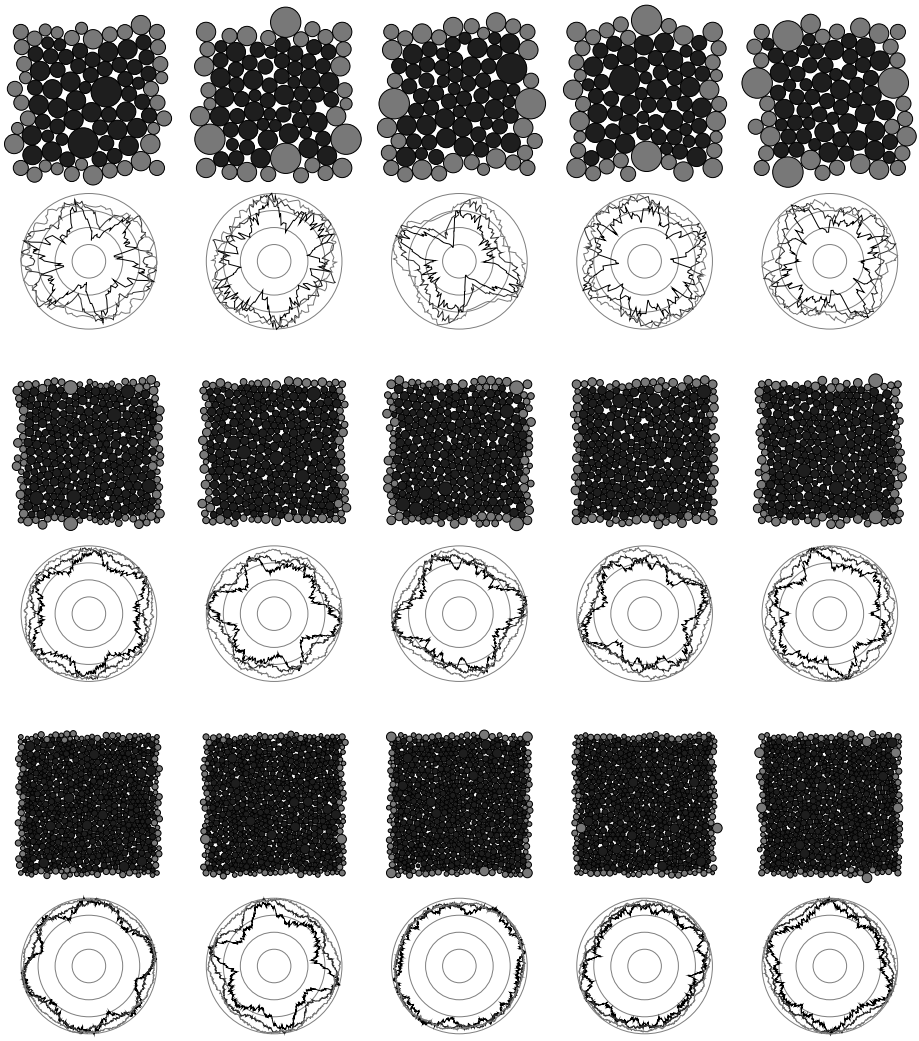

Figure 3: rves and their corresponding contact normal density functions. Black colored functions relate to an angle of influence equal to 10°, while blue and red colored functions correspond to an angle of influence equal to 20° and 30°, respectively. First set: Five rves, containing each 70 primary particles. Second set: Five rves, containing 350 primary particles. Third set: Five rves containing 700 primary particles (reproduced in color on p. 194).

5 Macroscale - finite element method

In the following we will consider a slope stability problem, first discussed in [ZP77]. The slope is subjected to dead load as well as a load originating from an massless strip footing

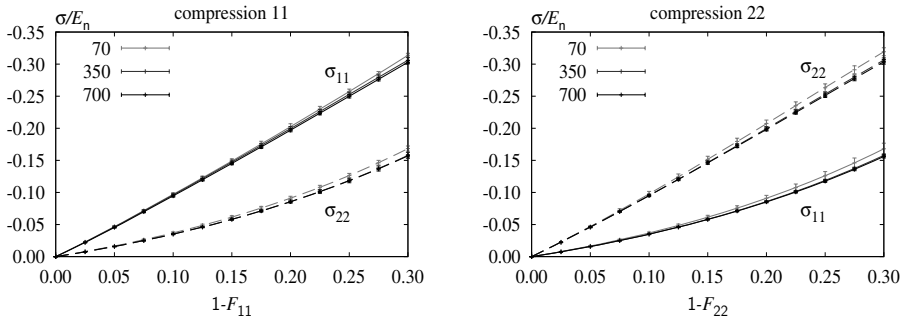

Figure 4: Averaged compression stress curves of the particle assemblies shown in Fig. 3. Error bars show the standard deviation. Left: Compression in 11 direction. Right: Compression in 22 direction. Solid lines relate to the Cauchy stress in 11 direction, while dashed lines are associated with the Cauchy stress in 22 direction.

subjected to an eccentric force. The dimensions of the problem as well as the applied boundary conditions are depicted in Fig. 6. Physical parameters are listed in Table 1. The footing has a width of $23.25\ m$. The dead load of the slope is applied in the first load step.

Table 1: Physical parameters for slope example

mass density	2.5E+03	$[kg/m^3]$
normal contact stiffness	2.8E+07	$[N/m^2]$
load	-4.0E+07	$[N]$

Twenty load steps are used to apply the eccentric force which is subjected to the massless strip footing. Fig. 7 shows a contour plot of the macroscopic von Mises stress. Four rves, connected to Gauss points of interest, are depicted, showing the force chain network in the deformed configuration. The convergence behavior of the relative energy norm for step two, six, ten, fifteen and eighteen is listed in Table 2.

6 Discussion

Inspired by the challenge of defining a complete multiscale calculation cycle, we presented a possibility to derive the macroscopic stress and tangent operator in the context of granular media. Both, the macroscopic stress and the macroscopic tangent operator are derived from the macroscopic strain energy, while the macroscopic strain energy itself depends on the prescribed macroscopic deformation gradient tensor. A complete two scale formulation was outlined, including different methods on the two scales, i.e., we do not apply the common FE^2. An example, showing the successful derivation and implementation was

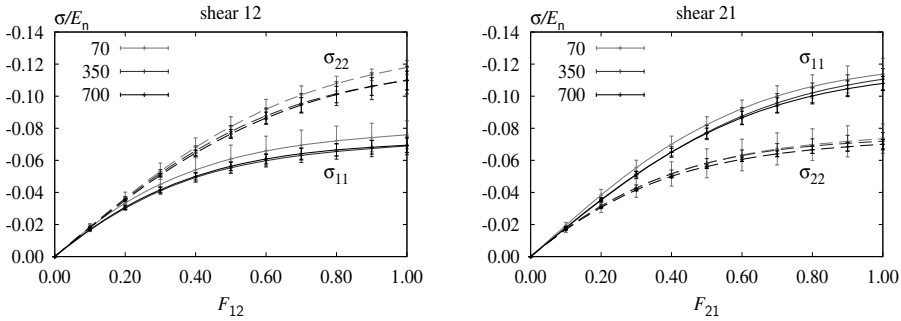

Figure 5: Averaged simple shear stress curves of the particle assemblies shown in Fig. 3. Error bars show the standard deviation. Left: Simple shear in 12 direction. Right: Simple shear in 21 direction. Solid lines relate to the Cauchy stress in 11 direction, while dashed lines are associated with the Cauchy stress in 22 direction.

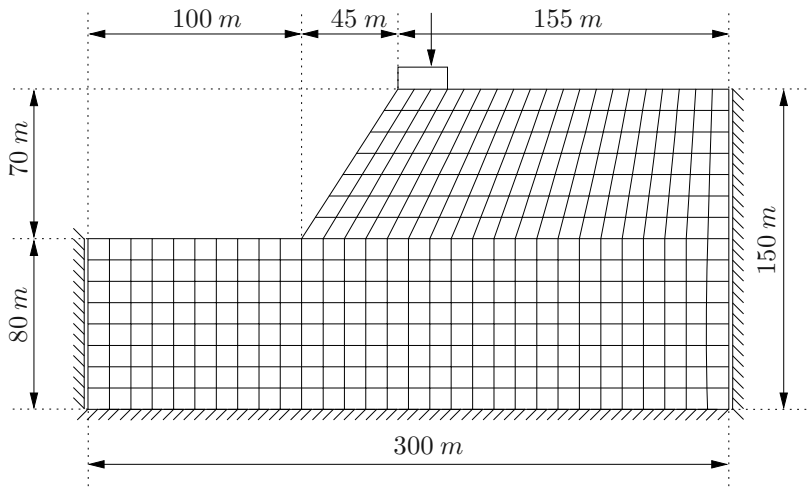

Figure 6: Undeformed mesh of the slope stability problem. Boundary conditions are depicted. 380 Q1 elements, containing each four Gauss points, are used. The massless footing is subjected to an eccentric force. The eccentricity is equal to $3.875\ m$.

granted, using a rve. Prior to the calculation, the representativeness was proofed by the use of a contact normal density function, showing the uniformity of the contact normals of the volume element. Stress curves, resulting from basic rve deformation, reinforce the prediction of the contact normal density functions. In case of the analysis of confined granular media, the results presented show an improvement with regards to the computational cost and the completeness of the algorithm. Thus, large scale computations of confined granular material are possible in the context of multiscale calculations. Finally, we would

Table 2: Convergence behavior of the relative energy norm

iter	step 2	step 6	step 10	step 15	step 18
1	1.000E+00	1.000E+00	1.000E+00	1.000E+00	1.000E+00
2	1.318E-02	3.341E-04	3.940E-04	1.322E-03	4.817E-03
3	1.947E-04	2.308E-08	1.503E-08	1.999E-07	3.816E-06
4	1.492E-07	7.110E-16	7.415E-16	6.114E-14	7.276E-12
5	5.846E-13	3.441E-26	5.014E-26	4.023E-26	5.932E-24
6	3.057E-26				

like to point out that although the presented algorithm has been proven highly effective and algorithmically efficient, it is far from being general enough to capture all characteristic effects in granular media.

Acknowledgment

The authors thank the German Research Foundation (DFG) for financial support within the DFG International Research Training Group 1131, "Visualization of Large and Unstructured Data Sets Applications in Geospatial Planning, Modeling and Engineering" at the University of Kaiserslautern. Furthermore, we kindly acknowledge the productive and inspiring collaboration with H. Hagen, A. Kerren, M. Schlemmer as well as C. Wagner from the AG Graphische Datenverarbeitung, Kaiserslautern, Germany.

References

[Bor15] M. Born. *Dynamik der Kristallgitter*. Teubner, 1915.

[Cau28a] A. L. Cauchy. De la pression ou tension dans un système de points matériels. *Exercises De Mathématiques*, pages 253–277, 1828.

[Cau28b] A. L. Cauchy. Sur l'équilibre et le mouvement d'un système de points matériels sollicités par des forces d'attraction ou de répulsion mutuelle. *Exercises De Mathématiques*, pages 227–252, 1828.

[CS78] P. A. Cundall and O. D. L. Strack. The Distinct Element Method as a Tool For Research in Granular Media. Technical report, Report to the National Science Foundation Concerning NSF Grant ENG76-20711, PART I, 1978.

[CS79] P. A. Cundall and O. D. L. Strack. The Distinct Element Method as a Tool for Research in Granular Media. Technical report, Report to the National Science Foundation Concerning NSF Grant ENG76-20711, PART II, 1979.

[Det06] J. P. Dettmar. *Static and Dynamic Homogenization Analyses of Discrete Granular and Atomistic Systems on Different Time and Length Scales*. PhD thesis, Institut für Mechanik (Bauswesen) , Universität Stuttgart, 2006.

[DKHR01] G. A. D'Addetta, F. Kun, H. J. Hermann, and E. Ramm. *From solids to granulates - discrete element simulations of fracture and fragmentation processes in geomaterials*, pages 231–258. Continuous and Discontinuous Modelling of Cohesive Frictional Materials, Lecture Notes in Physics 586. Springer-Verlag, Berlin, Germany, 2001.

[EDM01] W. Ehlers, S. Diebels, and T. Michelitsch. *Microscopic modelling of granular materials taking into account particle rotations*, pages 259–274. Continuous and Discontinuous Modelling of Cohesive Frictional Materials, Lecture Notes in Physics 586. Springer-Verlag, Berlin, Germany, 2001.

[ERDD03] W. Ehlers, E. Ramm, S. Diebels, and G. A. D'Addetta. From particle ensembles to Cosserat continua: Homogenization of contact forces towards stresses and couple stresses. *Int. J. Solids and Structures*, 40:6681–6702, 2003.

[Hil72] R. Hill. On constitutive macro-variables for heterogeneous solids at finite strain. *Proc. R. Soc. Lond. A*, 326:131–147, 1972.

[Hre41] A. Hrennikoff. Solution of Problems of Elasticity by the Framework Method. *ASME J. Appl. Mech.*, 8:169–175, 1941.

[KDHR00] E. Kuhl, G. A. D'Addetta, H. J. Herrmann, and E. Ramm. A comparison of discrete granular material models with continuous microplane formulations. *Granular Matter*, 2:123–135, 2000.

[KR96] N. P. Kruyt and L. Rothenburg. Micromechanical Definition of the Strain Tensor for Granular Materials. *ASME Journal of Applied Mechanics*, 118:706–711, 1996.

[MD04] C. Miehe and J. Dettmar. A framework for micro - macro transitions in periodic particle aggregates of granular materials. *Comput. Methods Appl. Mech. Engrg.*, 193:225–256, 2004.

[MKS07] H. A. Meier, E. Kuhl, and P. Steinmann. A note on the generation of periodic granular microstructures based on grain size distributions. *Int. J. Numer. Anal. Meth. Geomech.,(in press)*, 2007.

[MSW+07] H. A. Meier, M. Schlemmer, C. Wagner, A. Kerren, H. Hagen, E. Kuhl, and P. Steinmann. Visualization of Particle Interactions in Granular Media. *Submitted for publication*, 2007.

[Voi89] W. Voigt. Über die Beziehungen zwischen den beiden Elastizitätskonstanten isotroper Körper. *Wied. Ann.*, 38:573–587, 1889.

[Zoh05] T. I. Zohdi. Charge-induced clustering in multifield particulate flows. *Int. J. Numer. Meth. Engn.*, 62:870–898, 2005.

[ZP77] O. C. Zienkiewicz and G. N. Pande. Time-dependent multilaminate model of rocks - a numerical study of deformation and failure rock masses. *Int. J. Anal. Meth. Geomech.*, 1:219–247, 1977.

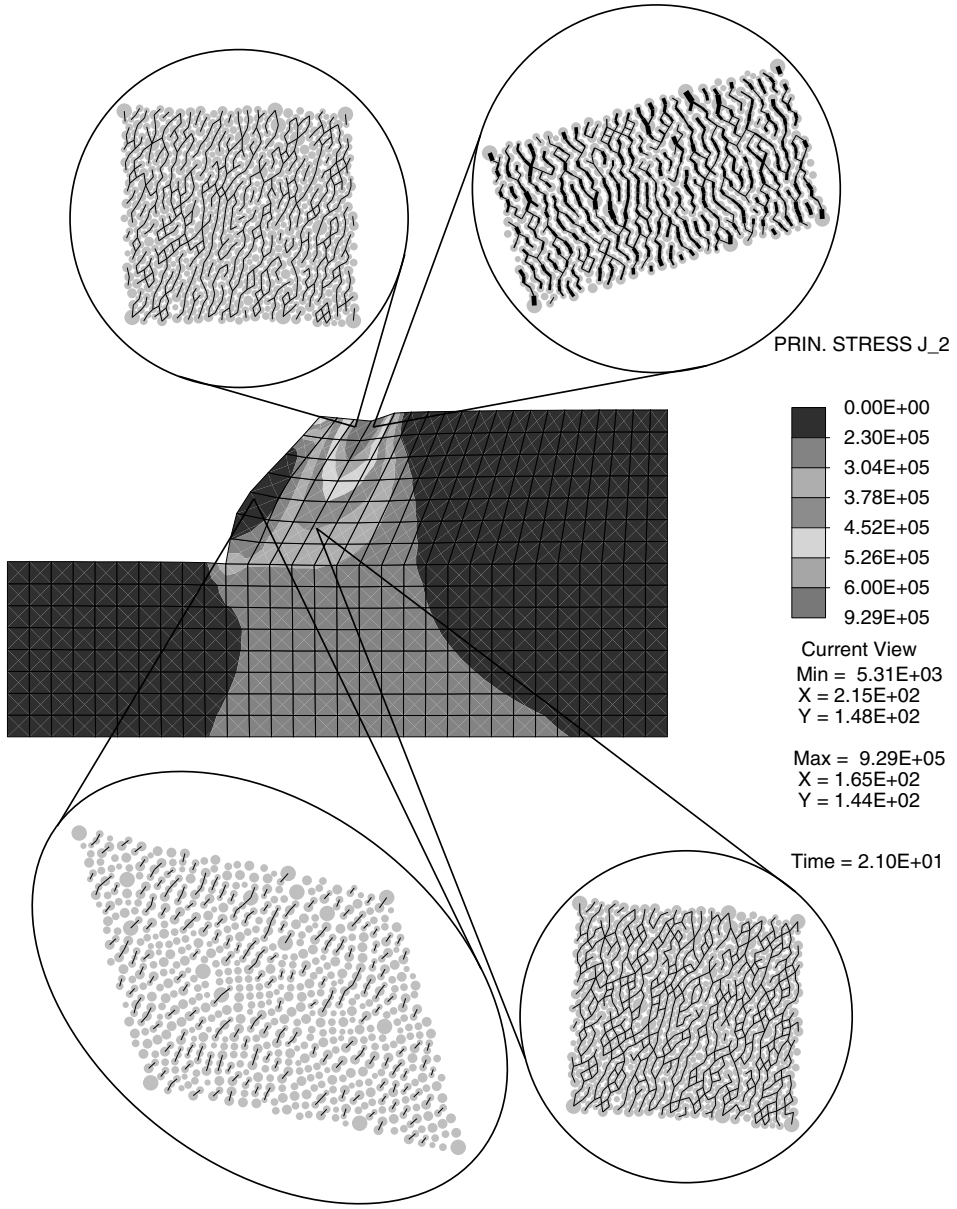

Figure 7: Final, deformed slope. The macroscopic von Mises stress is plotted. Initial localization is visible. Four deformed rves containing their contact networks are depicted. The tickness of the branches corresponds to the magnitude of the contact forces. The scaling factors for the branch thickness as well as for the deformation are equal for all four particle plots (reproduced in color on p. 195).